

www.acsaem.org Article

Unraveling the Electronic Heterogeneity and Inhomogeneity in Individual Perovskite CsPbBr₃ Nanowires

Yize Stephanie Li,* Shuang Liang, Tuong Trieu, Rahayana Ruth Bautista, and Zhiqun Lin



Cite This: ACS Appl. Energy Mater. 2022, 5, 4431-4438

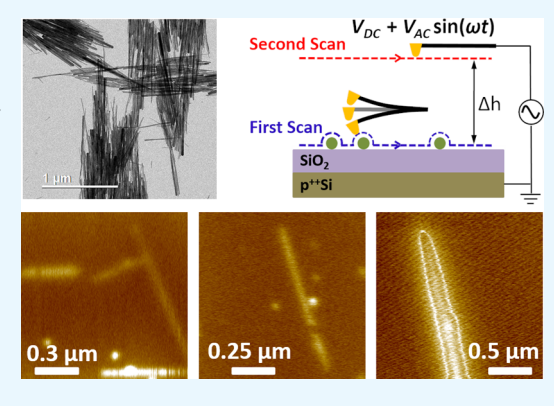


ACCESS I



Article Recommendations

ABSTRACT: Perovskite nanowires (NWs) have attracted significant attention due to their promise in optoelectronic applications. All-inorganic perovskite CsPbBr₃ NWs with a well-defined morphology were synthesized using a hot-injection approach. Subsequently, the electronic properties of individual CsPbBr₃ NWs spun onto SiO₂/Si substrates were scrutinized by contactless dielectric force microscopy (DFM). Ambipolar, n-type, and p-type responses were identified for different NWs, revealing the electronic heterogeneities of CsPbBr₃ NWs. Moreover, longitudinal electronic inhomogeneities were uncovered by the distinct DFM responses of different segments along some NWs whose diameters were 10–20 nm. In addition, DFM experiments unveiled transverse electronic inhomogeneities perpendicular to the length direction in some NWs whose diameters were 30–40 nm. This work demonstrates that the DFM technique is a powerful tool to probe the electronic heterogeneity and inhomogeneity in perovskite NWs, which



may have implications for the performance of materials and devices built upon them. In principle, our approach reported here could be extended to study the electronic properties of other one-dimensional metal halide perovskites.

KEYWORDS: metal halide perovskite, nanowire, dielectric force microscopy, electronic heterogeneity, electronic inhomogeneity

1. INTRODUCTION

Metal halide perovskites represent an emerging class of semiconducting materials that possess a spectacular array of intriguing optoelectronic properties, including a high defect a large absorption coefficient,² a fast charge carrier tolerance, mobility,³ and a size- and composition-dependent band gap.⁴ The past decade has witnessed many advances in metal halide perovskites for use in high-performance optoelectronic devices, including solar cells, ⁵⁻⁹ photodetectors, ^{6,10-12} photocathodes, ^{13,14} light-emitting diodes (LEDs), ^{3,9-12} and lasing. 10-12,15,16 Despite recent success in the shape-controlled synthesis of perovskite nanocrystals (NCs),¹⁷ only a limited number of morphologies have been achieved (e.g., nanocubes, 18 nanoplatelets, 19 nanosheets, 20 nanorods (NRs), 21 and nanowires (NWs)²²). Among various perovskite NCs, onedimensional (1D) NWs and NRs have garnered much interest due to their unique optoelectronic properties, including linearly polarized light emission, 23,24 enlarged photo absorption cross section, 25 improved charge transport, 26 and suppressed Auger recombination of excitons that greatly reduce the optical pumping threshold for stimulated emission.²⁷ 1D perovskite nanostructures (i.e., NWs and NRs) have been primarily synthesized using colloidal synthesis^{22,28} and surfactant-free substrate-assisted growth. ^{9,29,30} Notably, the colloidal synthesis of perovskite NWs affords a

high-quality and uniform morphology that renders the investigation into their intrinsic size- and shape-dependent properties and subsequent use in optoelectronic devices.²²

Charge transport in 1D perovskite nanostructures play a critical role in their device applications. 31,32 In some recent work, time-resolved photoluminescence (PL) was employed to extract the carrier lifetime 4 and carrier mobility 33 in CsPbBr $_3$ NWs. In other studies, metal contacts were made on an array or network of NWs, and current—voltage (I-V) characteristics were obtained from electrical transport measurements under dark and light conditions from which the photocurrent was determined, 4,34,35 and the defect density was calculated. Notably, I-V measurements on individual CsPbBr $_3$ NWs have also been achieved using conductive atomic force microscopy (AFM), which unveiled information about trap states. Nevertheless, it remains unknown whether the CsPbBr $_3$ NWs investigated in these works $^{4,33-36}$ were ambipolar, ptype, or n-type. In fact, few studies have addressed the type of

Received: December 20, 2021 Accepted: March 23, 2022 Published: April 5, 2022





majority carriers in 1D CsPbBr₃ nanostructures. 6,37-39 The prevailing method to identify the majority carrier and study the charge transport property of a semiconductor is to fabricate field effect transistors (FETs) and perform electronic transport measurements. In the article by Oksenberg et al., surfaceguided CsPbBr₃ NWs were synthesized on sapphire substrates using the non-catalyzed vapor solid growth method, an FET was fabricated on an array of NWs, and I-V measurements under different gate voltages were carried out.6 It was found that the array of NWs exhibited a p-type behavior. 6 More recently, Winterer et al. fabricated an FET device on a colloidal CsPbBr₃ NW film and observed a distinct p-type behavior.³⁷ In addition to a p-type characteristic, ambipolar behavior has also been reported in CsPbBr₃ NWs. 38,39 In the work of Meng *et* al., an FET device using a CsPbBr3 NW (with a diameter of around 150 nm) created by a Sn-catalyzed vapor-liquid-solid growth process was constructed, and the transfer characteristic was measured, which revealed an ambipolar attribute for pristine CsPbBr₃ NWs. ^{38,39} Unlike the devices studied in refs 6 and 37, which were fabricated on an array of NWs or a NW film, the FET device reported in refs 38 39, was fabricated on an individual NW. It is important to note that the limited reports on the polarity of CsPbBr₃ NWs in literature, particularly for individual NWs, are due largely to the challenge in fabricating FET devices on NWs. Moreover, the heterogeneity of nanomaterials and the challenge of distinguishing the influence of metal-nanomaterial contacts from the properties of the nanomaterials themselves could also make it difficult to interpret the transport measurement data.⁴⁰ It is therefore highly desirable to introduce a technique that does not require device fabrication, yet enables the investigation into the polarity and charge transport properties in 1D perovskite nanomaterials.

In this article, we report the scrutiny of the electronic properties of CsPbBr₃ NWs by employing contactless dielectric force microscopy (DFM). CsPbBr₃ NWs with diameters of 10–20 and 30–40 nm are examined. DFM images identify n-type NWs with electrons as the majority carriers, p-type semiconductor NWs with holes as the majority carriers, and ambipolar NWs with both electrons and holes as the majority carriers. DFM studies also reveal longitudinal inhomogeneities in CsPbBr₃ NWs with diameters of 10–20 nm and transverse inhomogeneities in CsPbBr₃ NWs with diameters of 30–40 nm.

2. MATERIALS AND METHODS

2.1. Materials. Cesium carbonate (Cs₂CO₃, 99%), oleic acid (OA, technical grade, 90%), octadecene (ODE, technical grade, 90%), oleylamine (OAm, technical grade, 70%), lead bromide (PbBr₂, 99.999%), ethyl acetate (anhydrous, 99.8%), and hexane (anhydrous, 95%) were all purchased from Sigma-Aldrich and used as received.

2.2. Synthesis of CsPbBr₃ **NWs.** The CsPbBr₃ NWs used in this study were synthesized by following the reported hot-injection approach. Specifically, the Cs-oleate precursor solution was synthesized by mixing 400 mg of Cs₂CO₃ and 1.5 mL of OA with 10 mL of ODE as the solvent in a three-neck flask, followed by being degassed and dried under vacuum at 120 °C, and then heated to 150 °C under inert gas protection until the solution became transparent. Afterward, 5 mL of ODE and 0.18 mmol PbBr₂ were loaded into a flask and degassed at 100 °C for 2 h after the injection of 1 mL of OA and 1 mL of OAm. Subsequently, under an inert gas atmosphere, the reaction system was further heated to 160 °C before the quick injection of 0.6 mL of the as-prepared Cs-oleate precursor solution. After 2 h, the reaction mixture was cooled by dipping into an icewater bath. The CsPbBr₃ NWs were then isolated from the solution

via centrifugation at 6000 rpm for 10 min and washed with ethyl acetate as the poor solvent and hexane as the good solvent multiple times. The diameter and length of the NWs can be readily tuned by varying the amount of ligands (i.e., OA and OAm) and reaction time, respectively.

2.3. Characterizations. The morphology of the as-prepared CsPbBr₃ NWs was investigated using a Hitachi HT7700 transmission electron microscope (TEM) operated at 120 kV. X-ray diffraction (XRD) spectra were obtained using a Panalytical Empyrean XRD system. The UV—vis spectra were collected using a Shimadzu UV-2600 spectrometer. The PL spectra were collected using a PerkinElmer LS 55 fluorescence spectrometer with the excitation wavelength at 365 nm.

2.4. Dielectric Force Microscopy. DFM is a contactless scanning force microscopy (SFM)-based technique that utilizes the 2ω channel in an electrostatic force microscopy setup to detect the dielectric polarization, and thus the electronic properties, of nanoscale materials. 40–42 In our prior work, using single-walled carbon nanotubes and ZnO as model systems, we showed that DFM allows the identification of semiconductor nanomaterials from metallic counterparts and the determination of the majority carrier type. 41 More quantitatively, we found that the DFM signals (*i.e.*, the dielectric responses) were strongly correlated with the electronic transport properties of nanomaterials. 40 Furthermore, due to the inherent nanoscopic spatial resolution of SFM-based techniques, it has been demonstrated that detecting local electronic inhomogeneities, including point defects and grain boundaries, was possible using DFM. 40

In this context, DFM was employed in our study to interrogate the electronic properties, in particular the majority carrier type and local electronic inhomogeneity, of CsPbBr₃ NWs spin-cast onto degenerately p-doped Si wafers with a 300 nm-thick thermal oxide layer. The DFM setup, including an external function generator (Keysight 33600A), a lock-in amplifier (SR830), and a home-made circuit, was built with a Park NX-10 atomic force microscope. Conductive AFM tips (MikroMasch NSC19/Cr–Au) with a typical resonance frequency of 65 kHz and a typical spring constant of 0.5 N/m were used as the probes. We used a double-pass imaging process, as shown in Figure 1a, where a topographic scan line was acquired in the first pass, and the oscillation of the cantilever at resonance frequency was turned off and the tip was lifted up to a height (typically 10–40 nm) in the second pass. ^{40,41} A bias voltage $V = V_{\rm DC} + V_{\rm AC} \sin(\omega t)$ from the function generator was applied to the conductive AFM tip only in the second pass. In this work, we used $V_{\rm AC} = 5-8$ V; $V_{\rm DC}$ was varied

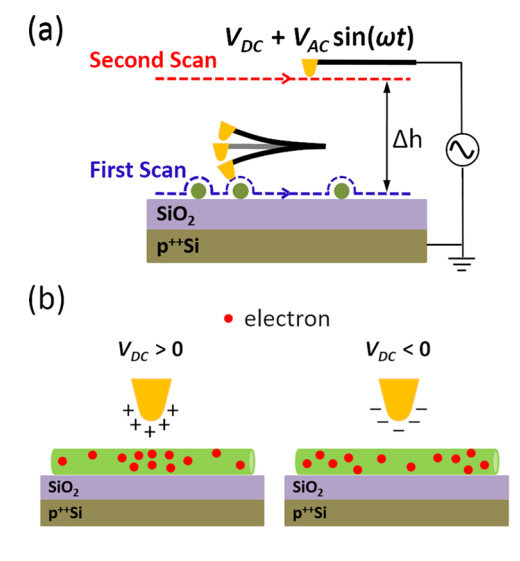


Figure 1. (a) Schematic illustration of a DFM experiment. (b) Schematic illustration on how $V_{\rm DC}$ modulates the local density of majority carriers (*i.e.*, electrons) in an n-type CsPbBr₃ NW.

between -3 and 3 V (or between -2 and 2 V), and ω was set to be 1 kHz. The role of the AC bias is to polarize the sample and result in an attractive dielectric force that oscillates in a 2ω frequency. The DC bias plays the role of a local gate, similar to the gate in an FET, which modulates the carrier density in the sample. Figure 1b shows how $V_{\rm DC}$ modulates the density of majority carriers, using an n-type CsPbBr3 NW as an example. For an n-type NW illustrated, the accumulation (depletion) of electrons below the conductive AFM tip in the presence of a positive (negative) $V_{\rm DC}$ results in a stronger (weaker) DFM response. For a p-type NW (not shown), on the other hand, the depletion (accumulation) of holes below the conductive AFM tip in the presence of a positive (negative) $V_{\rm DC}$ leads to a weaker (stronger) DFM response. 41,43 The 2ω component of the cantilever deflection signal, sampled by the lock-in amplifier, is recorded as the DFM image.

3. RESULTS AND DISCUSSION

3.1. Conventional Characterizations. As shown in Figure 2a,b, the TEM images of as-prepared CsPbBr₃ NWs

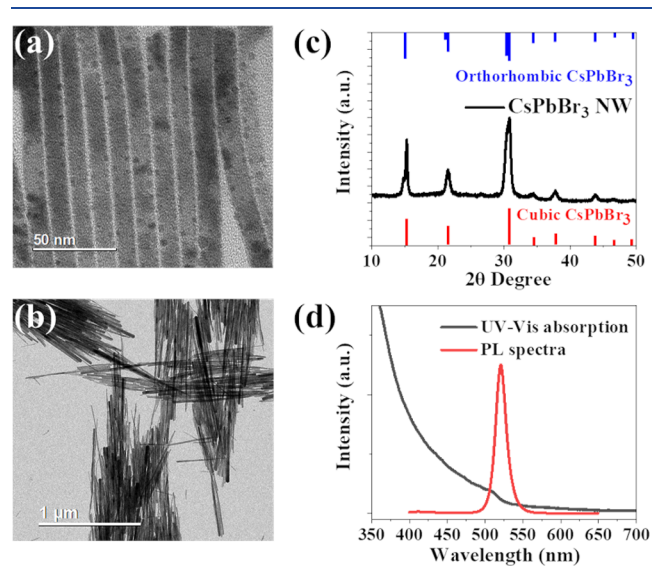


Figure 2. (a,b) TEM image of as-prepared perovskite $CsPbBr_3$ NWs. (c) XRD pattern of as-prepared $CsPbBr_3$ NWs; the red and blue lines represent the standard cubic phase and orthorhombic phase $CsPbBr_3$ in the literature. (d) UV-vis absorption and PL spectra of as-prepared $CsPbBr_3$ perovskite NWs.

reveal that CsPbBr3 NWs possess a uniform diameter and length of approximately 10 nm and 1 μ m, respectively. The appearance of small dots in the CsPbBr₃ NWs, shown in Figure 2a, results from the high-energy (i.e., 120 kV) electron beaminduced damage of the NWs during the TEM measurement. 10,44 The XRD pattern shown in Figure 2c suggests that the CsPbBr3 NWs are in either a cubic phase or a orthorhombic phase due to only a slight difference in their crystal structures, which is consistent with the literature. 22,45 The key difference in distinguishing the orthorhombic phase from the cubic phase is the splitting of the single peak into two peaks at ~30°. However, the small size of the CsPbBr₃ NWs leads to the appearance of peak broadening in this region, making it challenging to accurately determine the exact phase of the CsPbBr₃ NWs. Due to the asymmetric peak centered at around 30°, the as-prepared NWs likely manifested an orthorhombic phase.²² Furthermore, the optical properties of the CsPbBr3 NWs were scrutinized by measuring the UV-vis absorption and PL spectra in their colloidal solution. The

absorption onsets of CsPbBr₃ NWs shown in Figure 2d were found to be around 524 nm, while the peak position of PL was about 525 nm. The narrow PL emission (*i.e.*, full width at half maximum (FWHM); approximately 17 nm) of CsPbBr₃ NWs at room temperature shown in Figure 2d correlated well with the excitonic emission of CsPbBr₃ exhibiting a small degree of quantum confinement, which also suggests the high uniformity of as-prepared CsPbBr₃ NWs.²²

3.2. Electronic Heterogeneity. Figure 3a shows the topography and DFM images of a 1.2 μ m \times 1.2 μ m area on a SiO₂/Si substrate with four NWs, labeled as NW 1-NW 4. As revealed from the topography image, all four NWs had welldefined morphology and nearly uniform diameters. The diameters of these NWs were 15 \pm 1, 12 \pm 1, 11.5 \pm 1, and 12 ± 1 nm, respectively. The diameters of the NWs measured by DFM are slightly larger than the values obtained from TEM, possibly owing to the presence of an organic ligand layer outside the NWs, which is invisible under TEM but contributes to the height of the NWs determined by AFM. The strength of the DFM response is visualized from the color of the image: lighter colors indicate stronger responses and darker colors indicate weaker responses. NW 1 exhibited the weakest DFM response at $V_{\rm DC}$ = 0 V, and its DFM response at $V_{\rm DC}$ = 3 V appeared stronger than that at $V_{\rm DC}$ = -3 V, suggesting most likely an ambipolar NW with a stronger n-type response. 40,41 NW 2, on the other hand, displayed the strongest DFM response at $V_{\rm DC}$ = 3 V and the weakest DFM response at $V_{DC} = -3$ V, signifying an n-type NW.^{40,41} Similarly, we identified that NW 3 and NW 4 were n-type NWs. Notably, although the diameter of NW 4 was smaller than that of NW 1 and was the same as/similar to NWs 2-3, its DFM responses were significantly stronger than those of NWs 1-3. As we have showed in a prior work,⁴⁰ the DFM response of a 1D nanomaterial depends on the carrier density and mobility. The stronger DFM response from NW 4 indicates that an increase in the carrier density and/or mobility could play a more important role in influencing the electronic transport⁴⁰ than an increase in the diameter.

Figure 3b shows the topography and DFM images of a 2 μ m \times 2 μ m area on another SiO₂/Si substrate with five NWs from a different batch of CsPbBr₃ samples. Those five NWs, labeled as NW 5-NW 9, also had nearly uniform diameters. Their diameters were 12 ± 1 , 9 ± 2 , 16 ± 1 , 13 ± 1 , and 10 ± 1 nm, respectively. NW 5 exhibited the strongest DFM response at $V_{\rm DC}$ = -3 V and the weakest DFM response at $V_{\rm DC}$ = 0 V and was thus determined to be an ambipolar NW with a stronger p-type response. 40,41 NW 6 displayed the strongest DFM response at $V_{\rm DC}$ = -3 V and the weakest DFM response at $V_{\rm DC}$ = 3 V, so it was identified as a p-type NW. ^{40,41} NW 7 had much stronger DFM responses than the other four NWs. To qualitatively compare the DFM signals at different DC biases, increasing the range of the color scale was required so that the brightness of the DFM responses for NW 7 was reduced to the degree that the difference of DFM signals at different $V_{
m DC}$ could be distinguished by the image brightness (not shown). We found that NW 7 had the stronger DFM response at $V_{\rm DC}$ = -3 V and had the weakest DFM response at $V_{\rm DC}$ = 0 V, revealing an ambipolar NW with a stronger p-type response. Of course, with the increase of the color scale range, the DFM images of the other four NWs became hardly visible. The color scale for the DFM images shown in Figure 3b was chosen so that the DFM images of all five NWs were visible, and visually distinctive DFM responses at different DC biases were

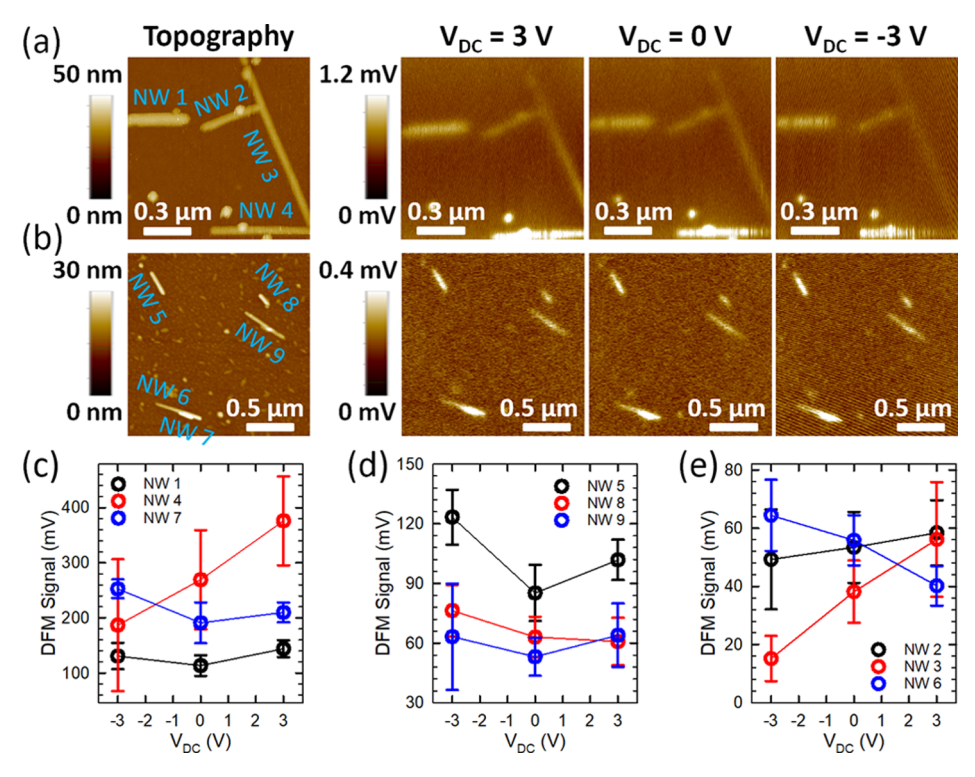


Figure 3. (a) Topographical image and dielectric response images at $V_{\rm DC}=3$, 0, and -3 V, respectively, of four CsPbBr₃ NWs (NWs 1–4) within a 1.2 μ m × 1.2 μ m area on a SiO₂/Si substrate. (b) Topographical image and dielectric response images at $V_{\rm DC}=3$, 0, and -3 V, respectively, of five CsPbBr₃ NWs (NWs 5–9) within a 2 μ m × 2 μ m area on a SiO₂/Si substrate. (c–e) DFM signal as a function of $V_{\rm DC}$ for all nine NWs shown in (a,b). The traces are grouped by the magnitudes of the DFM signals. For NW 4, the response from a dot on top of the NW was excluded when extracting the average DFM response. For NW 6, due to the partial overlap between its DFM signal and the much stronger DFM signal of NW 7, only its left portion was used when extracting its average DFM response.

displayed for all except NW 7. Similar to NW 6, NW 8 exhibited the strongest DFM response at $V_{\rm DC}=-3$ V and the weakest DFM response at $V_{\rm DC}=3$ V, suggesting a p-type NW. NW 9 had nearly identical DFM responses at $V_{\rm DC}=3$ and -3 V and had the weakest DFM response at $V_{\rm DC}=0$ V, implying an ambipolar NW with similar n-type and p-type responses.

Figure 3c-e shows the DFM signal extracted from the DFM images as a function of $V_{\rm DC}$ for all nine NWs showed in Figure 3a,b. The traces for NWs are grouped by the magnitudes of their DFM signals. Traces for NWs with strongest DFM responses are shown in Figure 3c, and traces for NWs with the weakest DFM responses are shown in Figure 3e. These quantitative plots also revealed that NW 1, NW 5, NW 7, and NW 9; NW 2, NW 3, and NW 4; and NW 6 and NW 8 were most likely ambipolar NWs; n-type NWs; and p-type NWs, respectively, as determined by a visual comparison of DFM images at different $V_{\rm DC}$ for each NW. The presence of all three types of responses (i.e., ambipolar response, n-type response, and p-type response) and the contrasting magnitudes in DFM signals from NWs of similar morphology suggest the electronic heterogeneity of CsPbBr₃ NWs in samples synthesized by the same solution-phase method.

The ratios of the maximum and minimum DFM responses (i.e., the dielectric response ratios) for NWs shown in Figure 3 ranged between 1.2 and 3.7. It has been determined that the gate modulation ratio of the source—drain current (i.e., $I_{\rm max}/I_{\rm min}$) of an FET device where a one-dimensional semiconductor material serves as the channel is correlated with the dielectric response ratio by a semi-logarithmic relation. ⁴⁰ If the NWs shown in Figure 3 were fabricated to FETs, the gate modulation ratios $I_{\rm max}/I_{\rm min}$ are then estimated to be in the

range of 15 to 5000, which further suggest the electronic heterogeneity of these CsPbBr₃ NWs.

The electronic heterogeneity of CsPbBr₃ NWs might be attributed to several origins. The ionic nature of a CsPbBr₃ perovskite crystal leads to intrinsic chemical instability and poor tolerance against moisture, polar solvent, heat, and light irradiation. 46 In this context, long alkyl-chain surface capping ligands (i.e., oleic acid and oleylamine in this study) are incorporated to stabilize the colloidal NWs and passivate their surface defects. 22,47 However, these ligands are only weakly bound on the perovskite NW surface in a dynamic equilibrium and thus are easily dissociated from the NW surface during storage and processing.⁴⁸ In addition to intrinsic structural instability, the incomplete surface coverage of ligands on the CsPbBr₃ NW owing to the ligand dissociation results in phase instability and formation of defects. As a result, the variation of surface chemistry in these NWs due to an uncontrollable extent of ligand dissociation contributes to distinctive structures, formation of defects of different types (e.g., Br vacancy vs Pb vacancy), and defect density in each individual NW, 49 thereby yielding different responses under DFM measurement and different majority carrier types observed. In addition, the introduction of an external electrical field during DFM measurement may lead to ion migration in the CsPbBr₃ NW, 50,51 which may cause the formation of defects and different responsive behaviors detected. 50,52

3.3. Electronic Inhomogeneity. The longitudinal electronic inhomogeneity is manifested by the presence of a segment with a much weaker DFM response compared to other parts of the NW, which was observed in several CsPbBr₃ NWs with diameters of 10–20 nm that we have studied. As an

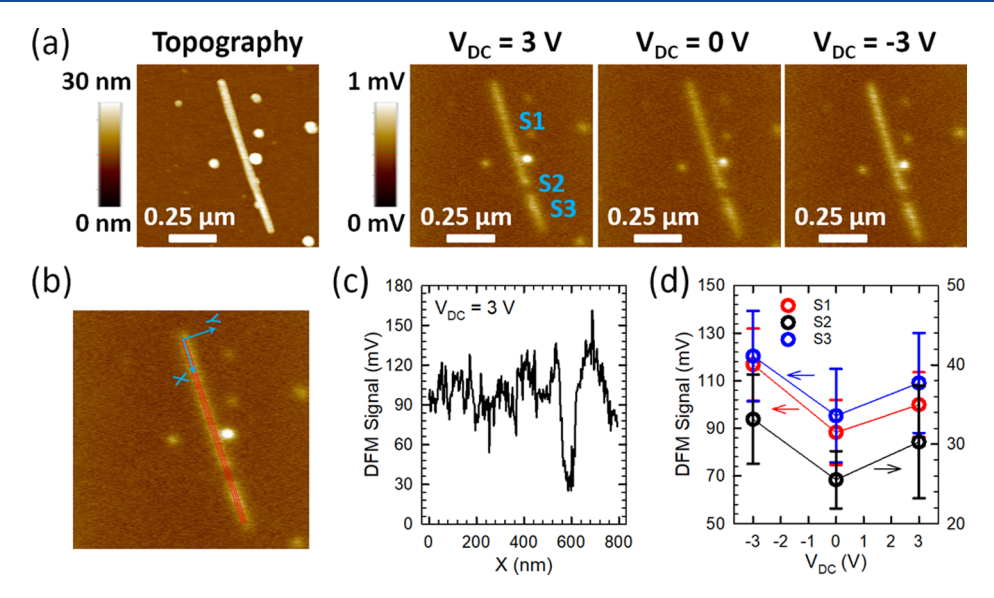


Figure 4. (a) Topographical image and dielectric response images at $V_{\rm DC}=3$, 0, and -3 V, respectively, of a CsPbBr $_3$ NW (diameter: 12.5 ± 1 nm) that exhibited longitudinal electronic inhomogeneities. (b) X-Y coordinate system whose origin is located at the top end of the NW and illustration of the selection of area within the NW for the extraction of the DFM signal as a function X (using the dielectric response image at $V_{\rm DC}=3$ V as an example). (c) DFM signal as a function of X extracted from the dielectric response image at $V_{\rm DC}=3$ V as illustrated in (b), where a deep valley was shown for S2. Similar features were also present for the DFM signal vs. X data extracted for $V_{\rm DC}=0$ and vs. Y (not shown). (d) DFM signal as a function of Y or segments S1, S2, and S3. Although all three segments exhibited ambipolar responses, the DFM signal from S2 was much weaker compared to those from S1 and S3.

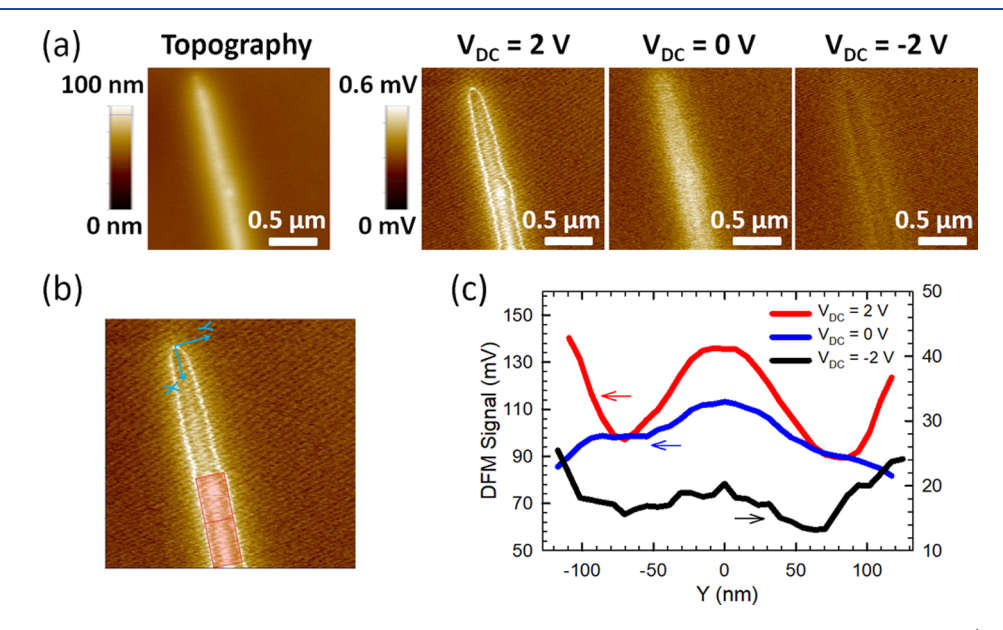


Figure 5. (a) Topographical image and dielectric response images at $V_{\rm DC}=2$, 0, and -2 V, respectively, of a CsPbBr $_3$ NW (diameter: 36 ± 1 nm) that exhibited transverse electronic inhomogeneities. (b) X-Y coordinate system whose origin is located at the top end of the NW and illustration of the selection of the area within the NW for extraction of the DFM signal as a function Y (using the dielectric response image at $V_{\rm DC}=2$ V as an example). (c) DFM signal as a function of Y for $V_{\rm DC}=2$, 0, and -2 V, respectively, extracted from the dielectric response images as illustrated in (b).

example, Figure 4a shows the topography and DFM images of a CsPbBr₃ NW with a diameter of 12.5 \pm 1 nm. Although the NW displayed a nearly uniform morphology along the entire NW, a small segment (labeled as S2) had a significantly weaker DFM response compared to the segments above (S1) and below (S3) it, at each $V_{\rm DC}$. We extracted DFM signals from the area enclosed in the red box along the NW length direction (*i.e.*, X-direction), as illustrated in Figure 4b. Figure 4c shows the DFM signal as a function of X for $V_{\rm DC}$ = 3 V, where the sharp valley came from S2. The DFM signal *versus* X for $V_{\rm DC}$ =

0 and -3 V exhibited similar valley features. We note that although the DFM response from S2 was too weak to be discernible from DFM images shown in Figure 4a, its DFM signals were non-zero at all three $V_{\rm DC}$. Figure 4d shows the DFM signal as a function of $V_{\rm DC}$ for each segment, indicating that the DFM responses of S1 and S3 were comparable and were 3–4 times stronger than that of S2. Ambipolar behaviors were observed for all three segments.

In addition to the longitudinal electronic inhomogeneity (i.e., electronic inhomogeneity along the length direction of a

NW), transverse electronic inhomogeneity (i.e., electronic inhomogeneity perpendicular to the length direction of a NW) has been revealed from DFM experiments on NWs with diameters of 30-40 nm. Figure 5a shows the topography and DFM images of a CsPbBr₃ NW with a diameter of 36 ± 1 nm. We note that the blurry boundary of the NW in the topographical image was an artifact caused by electrostatic charges. While this NW appeared featureless in the topographical image, its DFM images showed interesting inhomogeneous patterns in the transverse direction. In particular, at $V_{\rm DC}$ = 2 V, the DFM response at the center and the edges was significantly stronger than that of the regions in between. We note that the DFM features extended over a range that is much broader than the NW diameter, and the DFM broadening is also more significant than the tipconvolution-induced topography broadening, owing to the larger effective range of the probe-sample electrostatic interaction. As a result, the features shown in the DFM images are laterally broadened versions of the actual features. To provide the quantitative DFM response profile along the direction perpendicular to the length direction of this NW (i.e., Y-direction), we extracted DFM signals from the area enclosed in the red box, as shown in Figure 5b. Figure 5c shows the DFM signals as a function of Y for $V_{\rm DC}$ = 2, 0, and -2 V, respectively. At $V_{\rm DC}$ = 2 V, the DFM signal profile resembled a sinusoid with peaks at the center and edges and with valleys in between. At $V_{\rm DC}$ = 0 V, while the center still exhibited the strongest DFM response, the edges displayed the weakest DFM response. At $V_{\rm DC}$ = -2 V, on the other hand, while the center showed a stronger DFM response than the adjacent regions, the strongest DFM response appeared at the edges. Interestingly, while the traces at $V_{\rm DC}$ = 2 and -2 V showed well-defined local minima in DFM signals, the same regions appeared to be a plateau or a smooth transition between the maximum and minimum in the DFM signal vs.Y trace for $V_{\rm DC}$ = 0 V. The formation of a conspicuous transverse electronic inhomogeneity in some CsPbBr₃ NWs with relatively large diameters suggests that one needs to be cautious when using large-diameter CsPbBr₃ NWs for applications that require a good transverse electronic homogeneity.

4. CONCLUSIONS

In summary, we performed contactless DFM studies on perovskite CsPbBr₃ NWs synthesized using a hot-injection approach. Our observations of n-type, p-type, and ambipolar behaviors from different NWs revealed the heterogeneous nature of solution-phase synthesized CsPbBr₃ NWs. Longitudinal electronic inhomogeneities along the NW length direction were manifested by the presence of segments with contrasting DFM responses in some NWs with diameters of 10-20 nm. Furthermore, transverse electronic inhomogeneities perpendicular to the NW length direction were seen in some NWs with diameters of 30-40 nm. This work highlights a fast, contactless (i.e., non-destructive) approach to probe the electronic heterogeneity and inhomogeneity in CsPbBr₃ NWs, which could be applied to study other perovskite materials. It also suggests the importance of electronic characterizations on individual NWs prior to utilizing solution-phase synthesized NWs for device applications where a consistent major carrier type and/or longitudinal/transverse electronic homogeneity are desirable.

AUTHOR INFORMATION

Corresponding Author

Yize Stephanie Li — School of Natural Sciences, Mathematics, and Engineering, California State University, Bakersfield, California 93311, United States; ⊚ orcid.org/0000-0001-7510-1680; Email: yli11@csub.edu

Authors

Shuang Liang — School of Materials Science and Engineering, Georgia Institute of Technology, Atlanta, Georgia 30332, United States

Tuong Trieu — School of Natural Sciences, Mathematics, and Engineering, California State University, Bakersfield, California 93311, United States

Rahayana Ruth Bautista — School of Natural Sciences, Mathematics, and Engineering, California State University, Bakersfield, California 93311, United States

Zhiqun Lin — School of Materials Science and Engineering, Georgia Institute of Technology, Atlanta, Georgia 30332, United States; oorcid.org/0000-0003-3158-9340

Complete contact information is available at: https://pubs.acs.org/10.1021/acsaem.1c04016

Notes

The authors declare no competing financial interest.

ACKNOWLEDGMENTS

This work was supported by the National Science Foundation through grants DMR-1904042 and DMR-1903990.

REFERENCES

- (1) Kang, J.; Wang, L.-W. High Defect Tolerance in Lead Halide Perovskite CsPbBr₃. J. Phys. Chem. Lett. **2017**, *8*, 489–493.
- (2) Kazim, S.; Nazeeruddin, M. K.; Grätzel, M.; Ahmad, S. Perovskite as Light Harvester: A Game Changer in Photovoltaics. *Angew. Chem., Int. Ed.* **2014**, 53, 2812–2824.
- (3) Stranks, S. D.; Snaith, H. J. Metal-Halide Perovskites for Photovoltaic and Light-Emitting Devices. *Nat. Nanotechnol.* **2015**, *10*, 391–402.
- (4) Zhang, D.; Yang, Y.; Bekenstein, Y.; Yu, Y.; Gibson, N. A.; Wong, A. B.; Eaton, S. W.; Kornienko, N.; Kong, Q.; Lai, M.; Alivisatos, A. P.; Leone, S. R.; Yang, P. Synthesis of Composition Tunable and Highly Luminescent Cesium Lead Halide Nanowires through Anion-Exchange Reactions. *J. Am. Chem. Soc.* **2016**, *138*, 7236–7239.
- (5) Ma, T.; Wang, S.; Zhang, Y.; Zhang, K.; Yi, L. The Development of All-Inorganic CsPbX₃ Solar Cells. *J. Mater. Sci.* **2020**, *55*, 464–479.
- (6) Oksenberg, E.; Sanders, E.; Popovitz-Biro, R.; Houben, L.; Joselevich, E. Surface-Guided CsPbBr₃ Perovskite Nanowires with Size-Dependent Photoluminescence and Fast Photoconductive Response. *Nano Lett.* **2018**, *18*, 424–433.
- (7) Zhang, Q.; Yin, Y. All-Inorganic Metal Halide Perovskite Nanocrystals: Opportunities and Challenges. ACS Cent. Sci. 2018, 4, 668–679.
- (8) Im, J.-H.; Luo, J.; Franckevičius, M.; Pellet, N.; Gao, P.; Moehl, T.; Zakeeruddin, S. M.; Nazeeruddin, M. K.; Grätzel, M.; Park, N.-G. Nanowire Perovskite Solar Cell. *Nano Lett.* **2015**, *15*, 2120–2126.
- (9) Wong, A. B.; Lai, M.; Eaton, S. W.; Yu, Y.; Lin, E.; Dou, L.; Fu, A.; Yang, P. Growth and Anion Exchange Conversion of CH₃NH₃PbX₃ Nanorod Arrays for Light-Emitting Diodes. *Nano Lett.* **2015**, *15*, 5519–5524.
- (10) Zhang, D.; Yu, Y.; Bekenstein, Y.; Wong, A. B.; Alivisatos, A. P.; Yang, P. Ultrathin Colloidal Cesium Lead Halide Perovskite Nanowires. *J. Am. Chem. Soc.* **2016**, *138*, 13155–13158.

- (11) Deng, J.; Li, J.; Yang, Z.; Wang, M. All-Inorganic Lead Halide Perovskites: A Promising Choice for Photovoltaics and Detectors. *J. Mater. Chem. C* **2019**, *7*, 12415–12440.
- (12) Zhu, P.; Zhu, J. Low-Dimensional Metal Halide Perovskites and Related Optoelectronic Applications. *Infomatics* **2020**, *2*, 341–378.
- (13) Gao, L.-F.; Luo, W.-J.; Yao, Y.-F.; Zou, Z.-G. An All-Inorganic Lead Halide Perovskite-Based Photocathode for Stable Water Reduction. *Chem. Commun.* **2018**, *54*, 11459–11462.
- (14) Kim, I. S.; Pellin, M. J.; Martinson, A. B. F. Acid-Compatible Halide Perovskite Photocathodes Utilizing Atomic Layer Deposited TiO₂ for Solar-Driven Hydrogen Evolution. *ACS Energy Lett.* **2019**, *4*, 293–298.
- (15) Eaton, S. W.; Lai, M.; Gibson, N. A.; Wong, A. B.; Dou, L.; Ma, J.; Wang, L.-W.; Leone, S. R.; Yang, P. Lasing in Robust Cesium Lead Halide Perovskite Nanowires. *Proc. Natl. Acad. Sci. U.S.A.* **2016**, *113*, 1993–1998.
- (16) Xu, G.; Li, Y.; Yan, J.; Lv, X.; Liu, Y.; Cai, B. In-Plane Self-Assembly and Lasing Performance of Cesium Lead Halide Perovskite Nanowires. *Mater. Res. Lett.* **2019**, *7*, 203–209.
- (17) Shamsi, J.; Urban, A. S.; Imran, M.; De Trizio, L.; Manna, L. Metal Halide Perovskite Nanocrystals: Synthesis, Post-Synthesis Modifications, and their Optical Properties. *Chem. Rev.* **2019**, *119*, 3296–3348.
- (18) Pan, A.; He, B.; Fan, X.; Liu, Z.; Urban, J. J.; Alivisatos, A. P.; He, L.; Liu, Y. Insight into the Ligand-Mediated Synthesis of Colloidal CsPbBr₃ Perovskite Nanocrystals: The Role of Organic Acid, Base, and Cesium Precursors. *ACS Nano* **2016**, *10*, 7943–7954.
- (19) Shamsi, J.; Rastogi, P.; Caligiuri, V.; Abdelhady, A. L.; Spirito, D.; Manna, L.; Krahne, R. Bright-Emitting Perovskite Films by Large-Scale Synthesis and Photoinduced Solid-State Transformation of CsPbBr₃, Nanoplatelets. *ACS Nano* **2017**, *11*, 10206–10213.
- (20) Shamsi, J.; Dang, Z.; Bianchini, P.; Canale, C.; Di Stasio, F.; Brescia, R.; Prato, M.; Manna, L. Colloidal Synthesis of Quantum Confined Single Crystal CsPbBr₃ Nanosheets with Lateral Size Control up to the Micrometer Range. *J. Am. Chem. Soc.* **2016**, *138*, 7240–7243.
- (21) Gao, M.; Liu, H.; Yu, S.; Louisia, S.; Zhang, Y.; Nenon, D. P.; Alivisatos, A. P.; Yang, P. Scaling Laws of Exciton Recombination Kinetics in Low Dimensional Halide Perovskite Nanostructures. *J. Am. Chem. Soc.* **2020**, *142*, 8871–8879.
- (22) Zhang, D.; Eaton, S. W.; Yu, Y.; Dou, L.; Yang, P. Solution-Phase Synthesis of Cesium Lead Halide Perovskite Nanowires. *J. Am. Chem. Soc.* **2015**, *137*, 9230–9233.
- (23) Dou, Y.; Cao, F.; Dudka, T.; Li, Y.; Wang, S.; Zhang, C.; Gao, Y.; Yang, X.; Rogach, A. L. Lattice Distortion in Mixed-Anion Lead Halide Perovskite Nanorods Leads to their High Fluorescence Anisotropy. ACS Mater. Lett. 2020, 2, 814–820.
- (24) Li, Y.; Huang, H.; Xiong, Y.; Richter, A. F.; Kershaw, S. V.; Feldmann, J.; Rogach, A. L. Using Polar Alcohols for the Direct Synthesis of Cesium Lead Halide Perovskite Nanorods with Anisotropic Emission. *ACS Nano* **2019**, *13*, 8237–8245.
- (25) Li, J.; Jing, Q.; Xiao, S.; Gao, Y.; Wang, Y.; Zhang, W.; Sun, X. W.; Wang, K.; He, T. Spectral Dynamics and Multiphoton Absorption Properties of All-Inorganic Perovskite Nanorods. *J. Phys. Chem. Lett.* **2020**, *11*, 4817–4825.
- (26) Yang, D.; Li, P.; Zou, Y.; Cao, M.; Hu, H.; Zhong, Q.; Hu, J.; Sun, B.; Duhm, S.; Xu, Y.; Zhang, Q. Interfacial Synthesis of Monodisperse CsPbBr3 Nanorods with Tunable Aspect Ratio and Clean Surface for Efficient Light-Emitting Diode Applications. *Chem. Mater.* **2019**, *31*, 1575–1583.
- (27) Li, Q.; Yang, Y.; Que, W.; Lian, T. Size and Morphology-Dependent Auger Recombination in CsPbBr₃ Perovskite Two-Dimensional Nanoplatelets and One-Dimensional Nanorods. *Nano Lett.* **2019**, *19*, 5620–5627.
- (28) Imran, M.; Di Stasio, F.; Dang, Z.; Canale, C.; Khan, A. H.; Shamsi, J.; Brescia, R.; Prato, M.; Manna, L. Colloidal Synthesis of Strongly Fluorescent CsPbBr₃ Nanowires with Width Tunable Down to the Quantum Confinement Regime. *Chem. Mater.* **2016**, *28*, 6450–6454.

- (29) He, J.; Towers, A.; Wang, Y.; Yuan, P.; Jiang, Z.; Chen, J.; Gesquiere, A. J.; Wu, S.-T.; Dong, Y. In Situ Synthesis and Macroscale Alignment of CsPbBr₃ Perovskite Nanorods in a Polymer Matrix. *Nanoscale* **2018**, *10*, 15436–15441.
- (30) Zhou, H.; Yuan, S.; Wang, X.; Xu, T.; Wang, X.; Li, H.; Zheng, W.; Fan, P.; Li, Y.; Sun, L.; Pan, A. Vapor Growth and Tunable Lasing of Band Gap Engineered Cesium Lead Halide Perovskite Micro/Nanorods with Triangular Cross Section. ACS Nano 2017, 11, 1189—1195.
- (31) Qiu, T.; Hu, Y.; Xu, F.; Yan, Z.; Bai, F.; Jia, G.; Zhang, S. Recent Advances in One-Dimensional Halide Perovskites for Optoelectronic Applications. *Nanoscale* **2018**, *10*, 20963–20989.
- (32) Fu, Y.; Zhu, H.; Chen, J.; Hautzinger, M. P.; Zhu, X.-Y.; Jin, S. Metal Halide Perovskite Nanostructures for Optoelectronic Applications and the Study of Physical Properties. *Nat. Rev. Mater.* **2019**, *4*, 169–188.
- (33) Oksenberg, E.; Fai, C.; Scheblykin, I. G.; Joselevich, E.; Unger, E. L.; Unold, T.; Hages, C.; Merdasa, A. Deconvoluting Energy Transport Mechanisms in Metal Halide Perovskite using CsPbBr₃ Nanowires as a Model System. *Adv. Funct. Mater.* **2021**, *31*, 2010704. (34) Chen, J.; Fu, Y.; Samad, L.; Dang, L.; Zhao, Y.; Shen, S.; Guo, L.; Jin, S. Vapor-Phase Epitaxial Growth of Aligned Nanowire Networks of Cesium Lead Halide Perovskites (CsPbX₃, X = Cl, Br, I).
- Nano Lett. 2017, 17, 460–466. (35) Zhai, W.; Lin, J.; Li, C.; Hu, S.; Huang, Y.; Yu, C.; Wen, Z.; Liu, Z.; Fang, Y.; Tang, C. Solvothermal Synthesis of Cesium Lead Halide Perovskite Nanowires with Ultra-High Aspect Ratios for High-Performance Photodetectors. Nanoscale 2018, 10, 21451–21458.
- (36) Stern, A.; Aharon, S.; Binyamin, T.; Karmi, A.; Rotem, D.; Etgar, L.; Porath, D. Electrical Characterization of Individual Cesium Lead Halide Perovskite Nanowires Using Conductive AFM. *Adv. Mater.* **2020**, 32, 1907812.
- (37) Winterer, F.; Walter, L.; Lenz, J.; Seebauer, S.; Tong, Y.; Polavarapu, L.; Weitz, R. Charge Traps in All-Inorganic CsPbBr3 Perovskite Nanowire Field-Effect Phototransistors. *Adv. Electron. Mater.* **2021**, *7*, 2100205.
- (38) Meng, Y.; Lan, C.; Li, F.; Yip, S.; Wei, R.; Kang, X.; Bu, X.; Dong, R.; Zhang, H.; Ho, J. C. Direct Vapor-Liquid-Solid Synthesis of All-Inorganic Perovskite Nanowires for High-Performance Electronics and Optoelectronics. *ACS Nano* **2019**, *13*, 6060–6070.
- (39) Meng, Y.; Lai, Z.; Li, F.; Wang, W.; Yip, S.; Quan, Q.; Bu, X.; Wang, F.; Bao, Y.; Hosomi, T.; Takahashi, T.; Nagashima, K.; Yanagida, T.; Lu, J.; Ho, J. C. Perovskite Core-Shell Nanowire Transistors: Interfacial Transfer Doping and Surface Passivation. *ACS Nano* 2020, 14, 12749–12760.
- (40) Li, Y. S.; Ge, J.; Cai, J.; Zhang, J.; Lu, W.; Liu, J.; Chen, L. Contactless Probing of the Intrinsic Carrier Transport in Single-Walled Carbon Nanotubes. *Nano Res.* **2014**, *7*, 1623–1630.
- (41) Lu, W.; Zhang, J.; Li, Y. S.; Chen, Q.; Wang, X.; Hassanien, A.; Chen, L. Contactless Characterization of Electronic Properties of Nanomaterials Using Dielectric Force Microscopy. *J. Phys. Chem. C* **2012**, *116*, 7158–7163.
- (42) Zhang, J.; Lu, W.; Li, Y. S.; Cai, J.; Chen, L.; Wang, X.; Chen, L. Dielectric Force Microscopy: Imaging Charge Carriers in Nanomaterials without Electrical Contacts. *Acc. Chem. Res.* **2015**, *48*, 1788–1796.
- (43) Stabile, T.; Li, Y. S. Strained α -Sn Thin Films on Highly Lattice-Mismatched Ge Substrates. *Mater. Today Adv.* **2021**, *12*, 100189.
- (44) Jo, Y.-R.; Tersoff, J.; Kim, M.-W.; Kim, J.; Kim, B.-J. Reversible Decomposition of Single-Crystal Methylammonium Lead Iodide Perovskite Nanorods. ACS Cent. Sci. 2020, 6, 959–968.
- (45) Tong, Y.; Bohn, B. J.; Bladt, E.; Wang, K.; Müller-Buschbaum, P.; Bals, S.; Urban, A. S.; Polavarapu, L.; Feldmann, J. From Precursor Powders to CsPbX₃ Perovskite Nanowires: One-Pot Synthesis, Growth Mechanism, and Oriented Self-Assembly. *Angew. Chem., Int. Ed.* **2017**, *56*, 13887–13892.

- (46) Cottingham, P.; Brutchey, R. L. On the Crystal Structure of Colloidally Prepared CsPbBr₃ Quantum Dots. *Chem. Commun.* **2016**, 52, 5246–5249.
- (47) Krieg, F.; Sercel, P. C.; Burian, M.; Andrusiv, H.; Bodnarchuk, M. I.; Stöferle, T.; Mahrt, R. F.; Naumenko, D.; Amenitsch, H.; Rainò, G.; Kovalenko, M. V. Monodisperse Long-Chain Sulfobetaine-Capped CsPbBr₃ Nanocrystals and Their Superfluorescent Assemblies. ACS Cent. Sci. 2020, 7, 135–144.
- (48) De Roo, J.; Ibáñez, M.; Geiregat, P.; Nedelcu, G.; Walravens, W.; Maes, J.; Martins, J. C.; Van Driessche, I.; Kovalenko, M. V.; Hens, Z. Highly Dynamic Ligand Binding and Light Absorption Coefficient of Cesium Lead Bromide Perovskite Nanocrystals. *ACS Nano* 2016, 10, 2071–2081.
- (49) Dutta, S. K.; Bera, S.; Sen, S.; Pradhan, N. What Happens to Halide Perovskite Nanocrystals on TEM Grids upon Year-Long Ambient Storage? Surface Ligands versus Crystal Stability. *ACS Energy Lett.* **2022**, *7*, 773–777.
- (50) Yuan, Y.; Huang, J. Ion Migration in Organometal Trihalide Perovskite and Its Impact on Photovoltaic Efficiency and Stability. *Accounts Chem. Res.* **2016**, *49*, 286–293.
- (51) Holekevi Chandrappa, M. L.; Zhu, Z.; Fenning, D. P.; Ong, S. P. Correlated Octahedral Rotation and Organic Cation Reorientation Assist Halide Ion Migration in Lead Halide Perovskites. *Chem. Mater.* **2021**, 33, 4672–4678.
- (52) Zhang, B.-B.; Wang, F.; Zhang, H.; Xiao, B.; Sun, Q.; Guo, J.; Hafsia, A. B.; Shao, A.; Xu, Y.; Zhou, J. Defect Proliferation in CsPbBr₃ Crystal Induced by Ion Migration. *Appl. Phys. Lett.* **2020**, *116*, 063505.

□ Recommended by ACS

Mixed-Dimensional Heterostructure of CsPbBr3 Nanocrystal and Bi2O2Se Nanosheet

Ekashmi Rathore, Kanishka Biswas, et al.

NOVEMBER 30, 2021

THE JOURNAL OF PHYSICAL CHEMISTRY C

READ 🗹

Synthesis of Size-Controllable Self-Assembled CsPbBr3 Perovskite Nanowires: Implications for Photoemission with Less Recombination

Huazheng Li, Gaorong Han, et al.

MARCH 29, 2022

ACS APPLIED NANO MATERIALS

READ **C**

Chemically Spiraling CsPbBr3 Perovskite Nanorods

Suman Bera, Narayan Pradhan, et al.

SEPTEMBER 01, 2021

JOURNAL OF THE AMERICAN CHEMICAL SOCIETY

READ 🗹

Tuning Crystal Plane Orientation in Multijunction and Hexagonal Single Crystalline CsPbBr3 Perovskite Disc Nanocrystals

Suman Bera, Narayan Pradhan, et al.

APRIL 15, 2022

JOURNAL OF THE AMERICAN CHEMICAL SOCIETY

READ 🗹

Get More Suggestions >